Roll cells and disclinations in sheared nematic polymers

By J. J. FENG[1], J. TAO[1] AND L. G. LEAL[2]

[1]The Levich Institute for Physicochemical Hydrodynamics, City College of the
City University of New York, New York, NY 10031, USA

[2]Department of Chemical Engineering, University of California, Santa Barbara, CA 93106, USA

We use the Leslie–Ericksen theory to simulate the shear flow of tumbling nematic polymers. The objectives are to explore the onset and evolution of the roll-cell instability and to uncover the flow scenario leading to the nucleation of disclinations. With increasing shear rate, four flow regimes are observed: stable simple shear, steady roll cells, oscillating roll cells and irregular patterns with disclinations. In the last regime, roll cells break up into an irregular and fluctuating pattern of eddies. The director is swept into the flow direction in formations called 'ridges', which under favourable flow conditions split to form pairs of ± 1 disclinations with non-singular cores. The four regimes are generally consistent with experimental observations, but the mechanism for defect nucleation remains to be verified by more detailed measurements.

1. Introduction

Liquid-crystalline polymers (LCPs) have a more or less rigid backbone, and spontaneous alignment among the molecules gives rise to the nematic state (Donald & Windle 1992). A prominent feature of nematic LCPs is the numerous tortuous lines in the bulk that can be easily observed under a microscope (see e.g. Alderman & Mackley 1985). Known as disclinations, those are defect lines where the orientation of the polymer molecules changes abruptly. Disclinations can be eliminated by long-time annealing or by employing a strong magnetic field. However, once the material is subjected to a shear flow, disclination lines appear anew and, in time, multiply to form a dense network, dividing the LCP into the so-called polydomains. The shear-induced formation of orientational defects is a curious phenomenon of both scientific interest and practical importance. If LCPs are to be used as structural materials, a controlled spatial distribution of molecular orientation is highly desirable. Disclinations disrupt the orientation field and, along with macroscopic inhomogeneities that are prone to occur during processing (Donald & Windle 1992), are the main obstacles to putting nematic LCPs to wider applications.

Numerous observations of disclinations have been reported and many beautiful pictures published for both small-molecule liquid crystals and for liquid-crystalline polymers. However, the flow mechanism that has created disclinations remains obscure. Earlier work indicates a distinction between tumbling and flow-aligning nematics in the formation of defects (Gähwiller 1972; Manneville 1981). Recent experiments by Mather, Pearson & Larson (1996a,b), using the small-molecule 5CB and 8CB liquid crystals, established that disclinations nucleate in the bulk only if the liquid crystal

is a tumbler; in flow-aligning liquid crystals, bulk nucleation is never observed. Thus, flow-induced defects have been investigated mostly for tumbling nematics. Shear-flow experiments on initially defect-free samples (sometimes called monodomains) have been reported by several groups, using different anchoring conditions on the walls (Pieranski & Guyon 1976; Srinivasarao & Berry 1991; Müller, Stein & Winter 1996; Yan *et al.* 1994; Mather *et al.* 1996*b*). In the context of defect formation, the most detailed and revealing observations have come from a series of experiments by Larson & Mead (1992, 1993).

Liquid-crystalline polymers are characterized by two dimensionless measures of the shear rate. The first, known as the Ericksen number, provides a measure of the magnitude of viscous torques relative to elastic torques arising from spatial gradients in the average molecular orientation; the latter is generally specified by a unit vector n known as the *director*. The second dimensionless group is the Deborah number, and is the shear rate scaled by the orientational diffusivity of the rod-like LCP. Larson & Mead (1993) identified a series of transitions in the microstructural state of sheared nematic polymers, which they denoted as the Ericksen number and Deborah number cascades. The former covers lower shear rates where there is no distortion of the molecular orientation distribution around the director n. Starting with a monodomain with n initially aligned with the vorticity, they observed the birefringent patterns of poly(γ-benzyl-glutamate) (PBG) solutions through crossed polarizers. When the shear rate (or Ericksen number Er) exceeds a rather low threshold, regular parallel stripes appear along the flow direction. At higher shear rates, the stripes become irregular, and thick disclination lines somehow emerge between the stripes. With increasing shear rate, the stripes become more and more irregular, and the shape of the disclinations starts to fluctuate. Eventually, a chaotic pattern appears, producing the familiar polydomain texture. At still higher shear rates, one enters the Deborah number cascade. Now the dynamics is dictated by molecular viscoelasticity, and a defect-free monodomain reappears at sufficiently high Deborah numbers. We are interested in the genesis of defects in the Er cascade. The Deborah number cascade has been explored in a separate study (Sgalari, Leal & Feng 2000).

The origin of the birefringent stripes is well-known. Manneville & Dubois-Violette (1976) and Larson (1993) have shown that the simple shear flow of tumbling nematics is linearly unstable to the formation of streamwise *roll cells*. The secondary flow associated with those roll cells distorts the director orientation periodically along the vorticity direction, and hence produces the birefringent stripes. The counter-rotating pairs of rolls appear remarkably similar to the Taylor vortices in a Couette flow, and no such rolls appear in steadily sheared flow-aligning nematics (Pieranski & Guyon 1976). Larson & Mead's (1993) observations thus suggest that roll cells are central to the generation of disclinations in shear flows. However, the linear instability studies, of necessity, concern only infinitesimal disturbances, and cannot predict how they may grow into finite magnitude and eventually cause such severe distortions in the orientational field as to nucleate disclinations.

The current work is motivated by the gap between theory and experiment. Using direct flow simulations, we will follow the entire evolution of the roll cells, from onset to nonlinear growth and possibly to eventual breakup. In particular, we will establish a scenario for the nucleation of disclinations in simple shear flows. The rest of the paper is arranged as follows. Section 2 discusses the theoretical model and numerical method, along with the simplifying assumptions contained in each. Section 3 presents the numerical results, which are then compared with experiments in §4. There is general agreement, but the mechanism for defect nucleation cannot be

verified directly, and there is discrepancy in the location of defects. Conclusions are drawn in §5.

2. Theory and numerical methods

The simulations are based on the Leslie–Ericksen (LE) theory, which was developed for weak flows and small distortions such that the molecular orientation distribution retains its uniaxial equilibrium state (see e.g. de Gennes & Prost 1993). This may appear to be the obvious choice since the phenomena to be simulated occur in the Ericksen number cascade. However, the assumption of equilibrium orientation distribution becomes questionable near defect cores, where one may expect severe elastic distortions to reduce the molecular order and thus invalidate the LE theory. Fortunately, the defects observed in experiments are all 'thick lines', i.e. ± 1 defects of the 'escaped type' with a rather smooth core (de Gennes & Prost 1993). Therefore, the use of the LE model is justified provided the Deborah number remains small. Another reason for using the phenomenological LE theory is that molecular theories containing both molecular viscoelasticity and distortional elasticity are much more complex (Feng, Sgalari & Leal 2000). Indeed, such theories have so far only been used in planar flows (Kupferman, Kawaguchi & Denn 1999; Sgalari *et al.* 2000).

We should point out that many authors have done flow simulations using the LE theory. For example, Han & Rey (1994*a,b,c*, 1995) have carefully studied the shear flow between parallel planes. Since their interest was not in roll cells, no variation was allowed in the vorticity direction. Thus, their solutions feature the tumbling and twist instabilities which, given the proper boundary conditions, occur in a shearing flow prior to the formation of roll cells (Larson & Mead 1993). In §2.3 below, we will elaborate on these two instabilities as related to our boundary conditions.

2.1. *Governing equations and parameters*

The LE theory, as presented by de Gennes & Prost (1993), consists of two major equations:

$$n \times (h - \gamma_1 N - \gamma_2 n \cdot D) = 0, \tag{1}$$

$$\sigma = \sigma^{\mathrm{e}} + \alpha_1 D : nnnn + \alpha_2 nN + \alpha_3 Nn + \alpha_4 D + \alpha_5 nn \cdot D + \alpha_6 D \cdot nn. \tag{2}$$

Equation (1) states that the rotation of the director n is determined by the balance between an elastic torque and a viscous torque. h is the *molecular field* vector with the physical meaning of an elastic torque on the director. $N = \dot{n} - \Omega \cdot n$ is the rotation of the director with respect to the background fluid, with $\Omega = [(\nabla v)^{\mathrm{T}} - \nabla v]/2$ being the vorticity tensor and v being the velocity. $D = [(\nabla v)^{\mathrm{T}} + \nabla v]/2$ is the strain-rate tensor and γ_1 and γ_2 are viscosity constants. Equation (2) gives the stress tensor of the material, where σ^{e} is the Ericksen stress, and the α are Leslie coefficients related to the γ via

$$\gamma_1 = \alpha_3 - \alpha_2, \tag{3}$$

$$\gamma_2 = \alpha_3 + \alpha_2 = \alpha_6 - \alpha_5. \tag{4}$$

Larson (1993) proposed the following parameters for the 'typical nematic polymer' approximating several LCP solutions used in experiments:

$$(\alpha_1, \alpha_2, \alpha_3, \alpha_4, \alpha_5, \alpha_6) = (-45.91, -69.2, 3.13, 3.36, 60.15, -5.69)\,\mathrm{P},$$

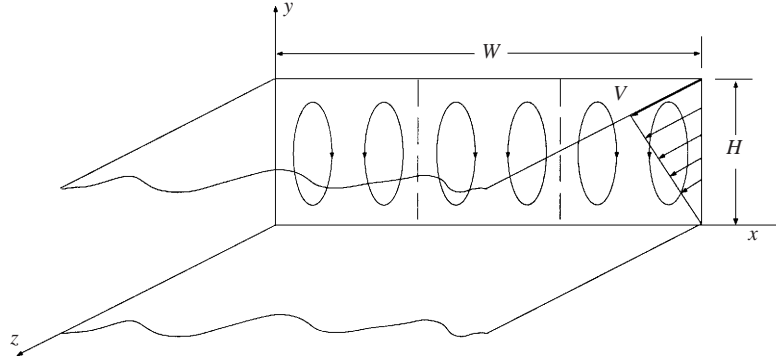$$(K_1, K_2, K_3) = (10^{-6}, 10^{-7}, 10^{-6})\,\mathrm{dyn},$$

FIGURE 1. The computational domain. The top wall moves in the z-direction with velocity V while the bottom wall is stationary.

where the K are the elastic constants for splay, twist and bend. In our simulations, we use the above α values, but assume elastic isotropy: $K = K_1 = K_2 = K_3 = 10^{-6}$ dyn. This one-constant approximation simplifies the algebra and the programming, and the use of a larger K_2 is not expected to affect the onset of roll cells appreciably (see Larson 1993). Now the molecular field h and the Ericksen stress σ^e have the following simple forms (de Gennes & Prost 1993):

$$h = K\nabla^2 n, \tag{5}$$

$$\sigma^e = -K\nabla n \cdot (\nabla n)^{\mathrm{T}}. \tag{6}$$

In making equations (1), (2), (5) and (6) dimensionless, we take the relative velocity V between the shearing plates to be the characteristic velocity, and the separation between the plates H to be the characteristic length. H/V is then the characteristic time. We further use the 'Newtonian' viscosity $\eta = \alpha_4/2$ as the characteristic viscosity, and define the Ericksen number as

$$Er = \frac{\eta V H}{K}. \tag{7}$$

The advantage of using η is that the equations of motion can be cast into a quasi-Stokes form (see equation (10) below). Based on different considerations, Larson (1993) used $\sqrt{-\alpha_2\alpha_4}$ as the characteristic viscosity and Larson & Mead (1993) used $\gamma_1 = \alpha_3 - \alpha_2$. Finally, based upon our choice of characteristic scales, the dimensionless constitutive equation and the equations of motion may be written as

$$n \times (Er^{-1}\nabla^2 n - \gamma_1 N - \gamma_2 D \cdot n) = 0, \tag{8}$$

$$\nabla \cdot v = 0, \tag{9}$$

$$\nabla p - \nabla^2 v = Er^{-1}\nabla \cdot [-\nabla n \cdot (\nabla n)^{\mathrm{T}}]$$
$$+ \nabla \cdot (\alpha_1 D : nnnn + \alpha_2 nN + \alpha_3 Nn + \alpha_5 nn \cdot D + \alpha_6 D \cdot nn), \tag{10}$$

where all viscosity coefficients have been scaled by η, and the pressure and the stress by $\eta V/H$. Fluid inertia is negligible compared with the viscous stress since the time scale for viscous dissipation is much shorter than that for the evolution of the flow. The latter time scale is determined by director rotation.

2.2. *Discretization*

We consider flow between two parallel planes, the lower being stationary and the upper translating in its own plane with velocity V. As shown in figure 1, our computational domain is a rectangle perpendicular to the flow direction (i.e. in the x, y-plane). We assume that neither the flow nor the orientation of $\boldsymbol{n}$ varies in the flow direction, and thus the rolls that will appear correspond to a swirling flow with three velocity components (u, v, w) depending on two spatial coordinates x and y. The issue of z-dependence will be discussed in §4.

The governing equations are discretized using finite difference on a uniform staggered grid with equal mesh size h along x and y. The u nodes are staggered by $h/2$ from the top and bottom walls, the v nodes staggered from the left and right boundaries, and w, p and $\boldsymbol{n}$ nodes staggered from all boundaries. This arrangement ensures accurate evaluation of the pressure gradient and strict enforcement of the incompressibility condition (Vanka 1986). The coupling between the pressure and velocity fields is treated using Patankar's SIMPLER scheme (Patankar 1980). Mesh refinement is done in one case for $N = 33$, 65 and 129 nodes along the y-direction. The difference between $N = 33$ and 65 is within 1%. Thus, we have used $N = 33$ in most calculations, although some cases are double-checked with $N = 65$.

The discretization of equation (8) requires special attention. Because of the constraint $\boldsymbol{n} \cdot \boldsymbol{n} = 1$, only two $\boldsymbol{n}$-components need to be computed at each point, and the torque balance is enforced along two directions in the plane orthogonal to $\boldsymbol{n}$. Since $\boldsymbol{n}$ changes in space and time, equation (8) is most conveniently discretized in a local principal coordinate system. Similar schemes have been used by Han & Rey (1994*a*) for nematics and by Feng & Leal (1997) for flexible polymers represented by a configuration tensor.

At every time step, we iterate among the governing equations (8)–(10) until convergence. The Poisson equations for pressure and the velocity components are solved using a multigrid method (see e.g. Hackbusch & Trottenberg 1982) and subroutines from the fast direct solver FISHPACK.

2.3. *Boundary conditions*

For velocity, the usual no-slip condition is applied on the top and bottom walls. For the director $\boldsymbol{n}$, the wall anchoring direction needs to be chosen carefully since it plays a vital role in the flow instability of tumbling nematics. If one imposes anchoring in the flow plane (the y, z-plane in figure 1), either perpendicular or parallel to the wall (known respectively as homeotropic and homogeneous anchoring), then a so-called *tumbling instability* may occur. This refers to the sudden rotation of $\boldsymbol{n}$ in the flow plane when the viscous torque overcomes the stabilizing elastic torque (Carlsson 1984; Burghardt & Fuller 1990). Zuniga & Leslie (1989*a,b*) recognized that such in-plane solutions may be unstable to out-of-plane disturbances in either the flow or the orientation. Their linear analysis predicts an out-of-plane *twist instability* at a critical shear rate which, depending on the viscosity parameters, may be higher or lower than that for the tumbling instability. Han & Rey (1994*a*) have constructed detailed bifurcation diagrams for these two instabilities. At higher shear rates, the director tips increasingly out of the flow plane and eventually becomes nearly aligned with the vorticity axis (x-axis in figure 1). The roll-cell instability referred to in the introduction occurs at even higher shear rates.

If $\boldsymbol{n}$ is anchored in the vorticity direction, however, the first instability that occurs is the onset of roll cells (Larson & Mead 1993). Hence, such anchoring is the most convenient for our purpose and has been used for all the roll-cell simulations

reported here. Partly to validate our numerical scheme and program, however, we also performed simulations with in-plane anchoring conditions. We ran dynamic simulations at several Er values astride the theoretical critical values of Zuniga & Leslie (1989a,b). In all cases, our results are consistent with the linear instability analysis for both tumbling and twist instabilities.

The sidewalls in figure 1 introduce two numerical problems. The first concerns what channel width to use. Since the aspect ratio of the rolls is unknown *a priori*, and only an integer number of rolls can be simulated within the width W, we cannot capture the exact dominant wavenumber with certainty. Instead, we have used wide domains to reduce the error in the wavenumber. Results show that $W = 8$ and 16 yield essentially the same wavenumber and hence $W = 8$ is used for most of the calculations (recall that W is scaled by the gap H between the plates). The second issue is the boundary conditions on the sidewalls. Periodic boundary conditions, as it turns out, introduce an artificial 'cross-flow instability', with the top half of the domain flowing to the left (or right), and the bottom half to the right (or left). Apparently, impermeable sidewalls are necessary to ensure roll cells in the simulations. This may also be the case in reality since sidewalls are always present. Based on the conditions at cell boundaries suggested by the linear instability analysis of Larson (1993), we have used slippery wall conditions, with $u = 0, \partial v/\partial x = 0$ and $\partial w/\partial x = 0$ on the sidewalls. The director is anchored in the x-direction, perpendicular to the sidewalls.

3. Numerical results

Initially, the director field is uniform with $\boldsymbol{n} = (1, 0, 0)$ everywhere. Then we supply a small random disturbance of magnitude 10^{-4} to the director field and start the shear flow. Via a coupling between the flow and the orientation, the disturbance may either die out or grow into an instability. Dynamic simulations of this process show that four different flow regimes appear for increasing Er:

  A. Stable simple shear
  B. Steady roll cells
  C. Oscillating roll cells
  D. Irregular patterns with disclinations.

We will discuss each in detail. The critical Er values separating the regimes are determined with a margin of error of 5. Animated videos for some of the solutions are available at http://lisgi1.engr.ccny.cuny.edu/~feng/resb.html.

3.1. *Stable simple shear* ($Er < 55$)

When the Ericksen number is below a critical value of 55, the initial disturbance dies out and the simple shear flow, with the director in the 'log-rolling' state, is stable.

3.2. *Steady roll cells* ($55 < Er < 85$)

In this regime, counter-rotating pairs of rolls appear and grow monotonically to a steady state. Figure 2 illustrates this process for $Er = 60$. The rolls first take shape at approximately 80 strain units (or dimensionless time $t = 80$); the velocity of the secondary flow is extremely weak at this stage (figure 2a). The final steady state is approached at some 400 strain units, the secondary flow attaining a magnitude of roughly 1% of that of the primary flow (figure 2b). In the steady-state director field (figure 2c), non-zero components n_z and n_y represent, respectively, deviations from the wall anchoring direction $\boldsymbol{n}_a = (1, 0, 0)$ within and out of the sample plane (the x, z-plane in figure 1). A comparison between the flow and director fields shows
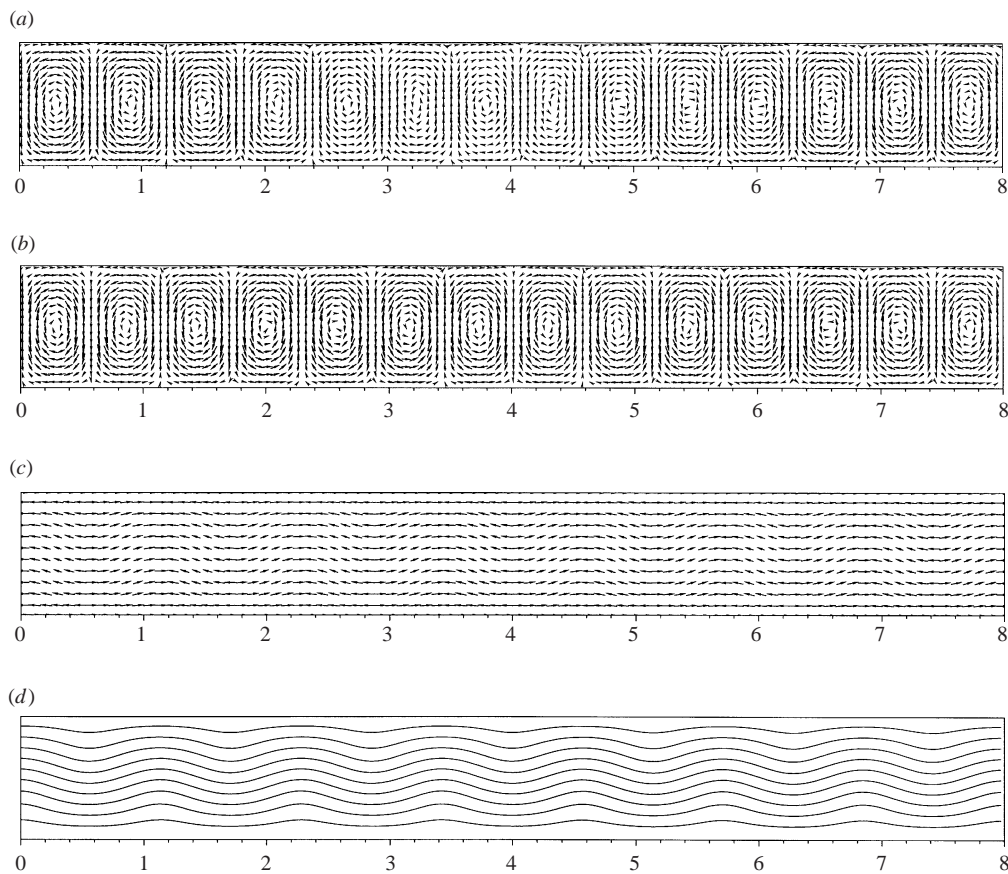
(a)

(b)

(c)

(d)

FIGURE 2. The growth of roll cells at $Er = 60$. (a) Vector plot of the velocity components u and v showing the swirling 'eddies' for the nascent rolls at time $t = 80$. The magnitude of u and v are on the order of 10^{-5}. (b) The steady-state rolls at $t = 400$, with wavenumber $q_x = 0.875$ and aspect ratio 0.571; u and v are on the order of 0.01. (c) The steady-state director field at $t = 400$. The arrow points out of the page and a short line segment indicates a large n_z-component. (d) Isolines of the velocity component w, whose variation is in concert with u and v.

that the greatest deviation of $\boldsymbol{n}$ from $\boldsymbol{n}_a$ occurs at the core of the swirling 'eddies', where $\boldsymbol{n} = (0.632, 0.23, 0.74)$ is most aligned with the flow direction. In the region between rolls, $\boldsymbol{n}$ remains largely undisturbed. This pattern is consistent with the fact that the secondary flow exerts the greatest shear at the core and virtually no shear at the boundaries between rolls (cf. figure 2b). Figure 2(d) shows contours of the dimensionless velocity component w, which also varies periodically across the rolls. It is greatest at those roll boundaries that have a downward v, and smallest where v goes upward. This is evidently a result of the secondary flow transporting faster fluid downward in the first case, and slower fluid upward in the second.

A notable feature of the evolution of the rolls is its uneventfulness. The nonlinear growth of the instability consists in monotonic increases of the roll 'strength', both in terms of the recirculating velocity and the director tipping. The rolls keep the same wavenumber ($q_x = 0.875$ for $Er = 60$), and no dramatic episodes, such as the modal interaction envisioned by Larson (1993), take place. Therefore, the steady-state rolls appear very similar to the pictures suggested by Larson's (1993) linear instability
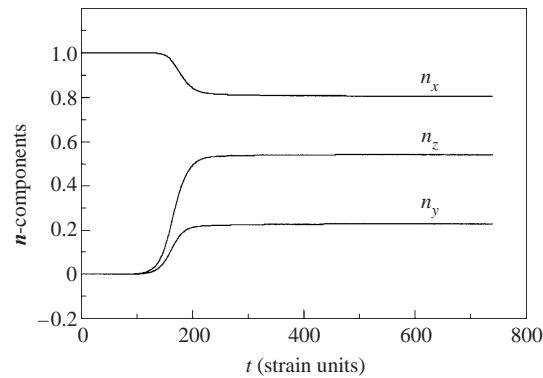
FIGURE 3. The history of the **n**-components at $(x, y) = (2, 0.25)$ at $Er = 60$. Initially **n** is along the x-axis. Deviations start at $t \approx 80$ when the rolls form, and grow monotonically till the steady state at $t \approx 400$.
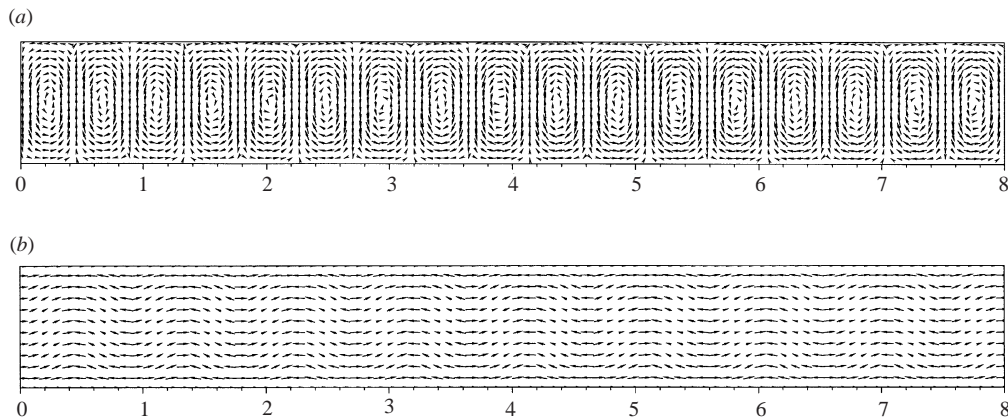
(*a*)

(*b*)

FIGURE 4. The fully grown roll cells at $t = 80$ for $Er = 100$. (*a*) The velocity field. (*b*) The director field. The wavenumber is $q_x = 1.0625$ and the aspect ratio of the roll is 0.471. At the core of the eddies **n** = (0.42, 0.24, 0.88).

analysis. In fact, all the qualitative features discussed in the last paragraph also apply to the infinitesimal roll cells of Larson (1993). This lack of drama is accentuated by figure 3, showing the history of the director components at $(x, y) = (2, 0.25)$, an arbitrarily chosen spatial point. A log-log plot (not shown here) indicates that the disturbances grow exponentially up to $t = 160$; within this time the instability remains essentially linear.

At higher Er in this regime, the qualitative features are the same, although the rolls develop more quickly and are stronger with more severe distortion of the **n**-field. The rolls are narrower, with the wavenumber q_x increasing with Er. This effect will be revisited in §4.

3.3. *Oscillating roll cells* $(85 < Er < 145)$

In this regime, the initial stage of roll formation and growth is similar to the last regime. Given the higher Er, the dominant wavenumber is larger (the cells are narrower), and the growth is more rapid. Figure 4 shows the more or less fully grown roll cells at $t = 80$ for $Er = 100$. Again the most severe tipping of the director occurs
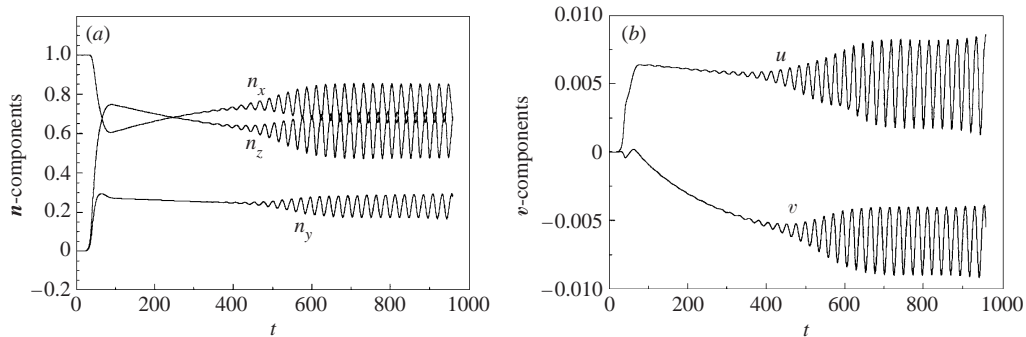
FIGURE 5. Evolution of the roll cells into an oscillating pattern at $Er = 100$. (a) History of $\boldsymbol{n}$-components at $(x, y) = (2, 0.25)$. (b) History of velocity components u and v; w behaves similarly and is omitted. The period of oscillation is approximately 26 strain units.
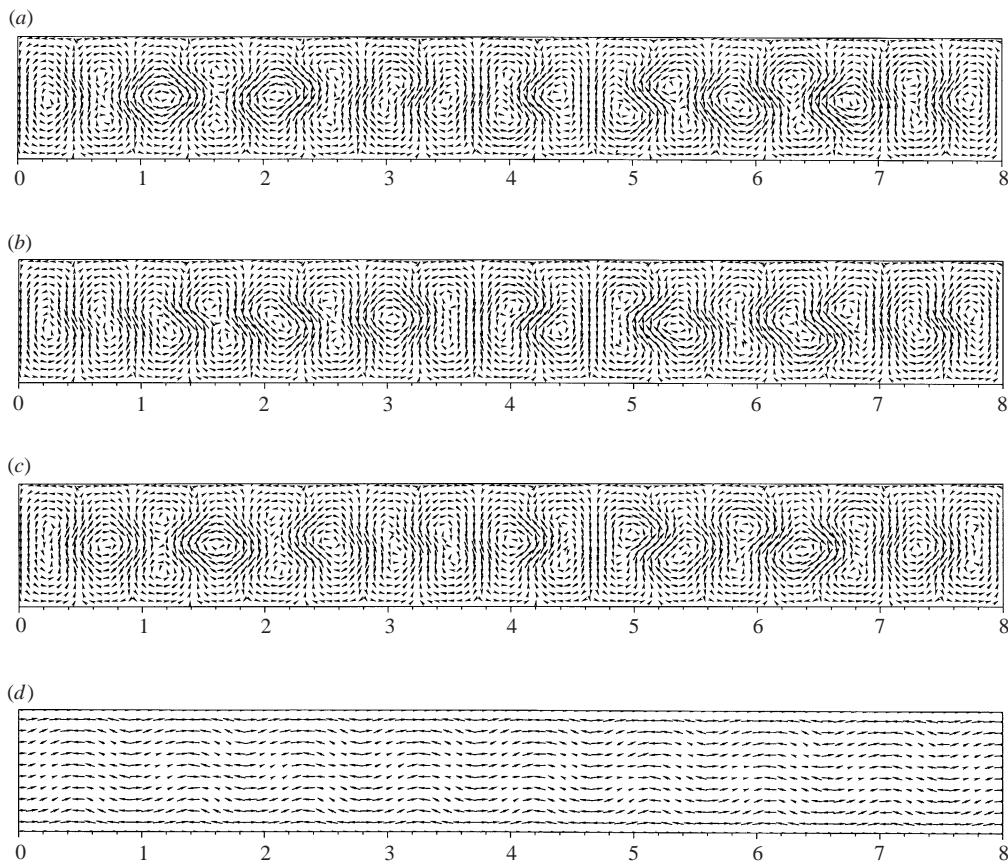

FIGURE 6. One half-cycle of the oscillating roll cells for $Er = 100$. The velocity field at (a) $t = 864$; (b) $t = 870$; (c) $t = 876$. (d) The director field at $t = 876$.

at the core of the eddies: $\boldsymbol{n} = (0.42, 0.24, 0.88)$; there the flow sweeps $\boldsymbol{n}$ mostly into the flow direction despite the wall anchoring in the x-direction.

The rolls shown in figure 4 do not represent a steady state, however. The flow continues to evolve and a secondary instability sets in the form of growing oscillations
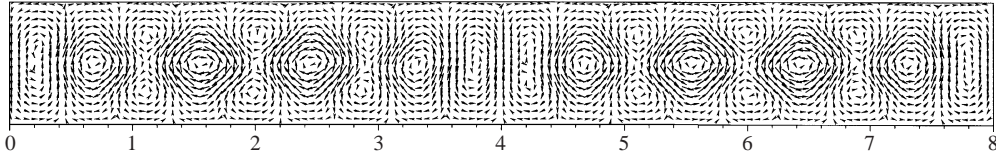
FIGURE 7. Oscillating roll cells resulting from a sinusoidal initial disturbance of amplitude 10^{-4} and wavenumber 1. $t = 864$, $Er = 100$. This solution is similar to that in figure 6, but with a larger wavenumber $q_x = 1.125$ and a shorter period (≈ 22 strain units).

within the (x, y)-plane. The rolls eventually evolve into a solution periodic in time and quasi-periodic in space. The entire process is illustrated by the histories of $\boldsymbol{n}$- and $\boldsymbol{v}$-components at a fixed spatial point (figure 5). To understand what happens within each cycle of oscillation, we compare in figure 6 the roll cells at different times covering one half-cycle.

In figure 6(*a*) it can be seen that the rolls are no longer rectangular with straight edges as in figure 4. Instead, there is an alternating pattern of 'dumbbells' and 'wrist-watches'. There are also variations along the width of the domain, with the two shapes distinct near the sides and less recognizable in the middle. In figure 6(*b*), the distinct dumbbells and wrist-watches are propagating toward the centre of the domain. Near the left and right sides, neighbouring rolls interact and become skewed, with a strong flow crossing their boundaries at roughly 45°. By the end of the half-cycle (figure 6*c*), distinct dumbbells and watches have reappeared near the outer edges of the domain, while the middle now has skewed rolls. But the dumbbells and watches have switched position between figure 6(*a*) and figure 6(*c*). Now the temporal behaviour of the oscillating roll cells is clear. Each cell splits into a dumbbell, which becomes skewed and then contracts back into a wrist-watch. The wrist-watch then skews and stretches into a dumbbell, and the cycle repeats. All cells oscillate with the same period (roughly 26 strain units in this case), but there is a phase difference across the width of the domain; hence the lack of perfect periodicity along the horizontal x-direction at any time.

The director field in figure 6(*d*) forms an intriguing contrast to the flow field in figure 6(*c*). For dumbbells, the greatest tipping of $\boldsymbol{n}$ occurs at the centre, i.e. in the thin 'waist' between the two bulbs; there $\boldsymbol{n}$ is very nearly aligned with the flow. Thus, the director field suggests one whole cell while the flow field has the split pattern. For the wrist-watch, on the other hand, the greatest tipping occurs above and below the centre; the director pattern suggests roll splitting, again contrary to the flow field. We do not have an explanation for the apparent discrepancy.

Another notable feature of the periodic solution is its non-uniqueness. The solution discussed so far has evolved from a spatially random perturbation of the log-rolling state. If we instead use a sinusoidal initial disturbance, a different periodic solution results, with a slightly larger wavenumber and a shorter period of oscillation (figure 7). Figure 8 compares the two solutions through the history of n_x. With the sinusoidal initial disturbance, a roll-cell pattern with the *forcing wavenumber* $q_x = 1$ develops first and persists until $t \approx 200$. A period of violent re-adjustment ensues, out of which a periodic solution emerges with a different wavenumber (cf. figure 7). The two curves in figure 8 show no signs of converging into one, and the solutions depicted in figures 6 and 7 are evidently distinct solutions. Therefore, there are at least two neighbouring modes of disturbance that are viable; either may prevail in the final solution depending on the initial condition. There may be more competing solutions.
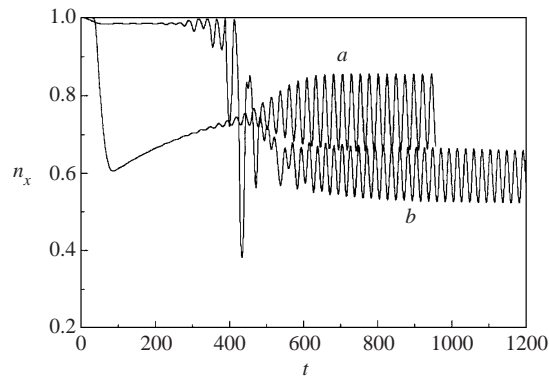
FIGURE 8. Multiple solutions as seen from the history of n_x at $(x, y) = (2, 0.25)$. $Er = 100$. Curve (*a*) derives from a random initial disturbance whereas curve (*b*) from a sinusoidal initial disturbance.
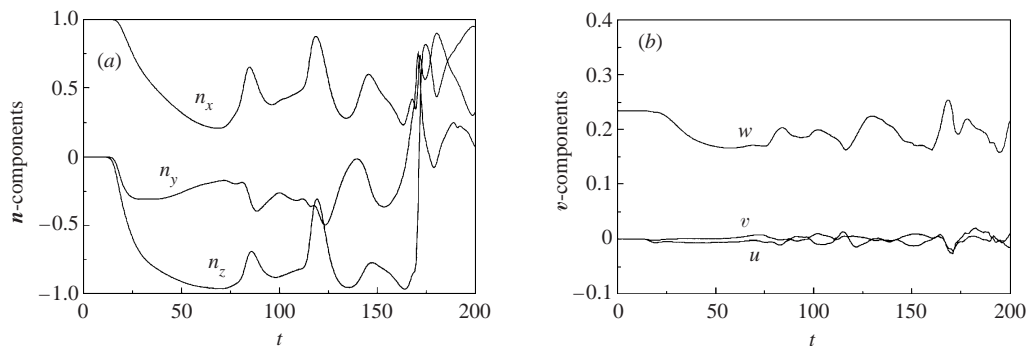

FIGURE 9. The histories of $\boldsymbol{n}$- (*a*) and $\boldsymbol{v}$- (*b*) components at $(x, y) = (2, 0.25)$ for $Er = 200$. Though not obvious in the plots, the rolls are fully grown by $t = 30$, and then break up and become irregular.

This non-uniqueness is not surprising since Larson's (1993) linear instability analysis has predicted a wide spectrum of unstable modes, especially at higher Er. In the previous regime of steady roll cells, numerical experiments failed to uncover multiple solutions. This does not rule out their existence, however. For example, our code assumes an integer number of cells in the domain, and thus could not distinguish two modes with slightly differing wavenumbers.

Finally, one may note that the two cells at the left and right ends are forced to have a straight edge next to the slippery sidewalls. This sidewall effect may play a role in the phase difference across the width of the domain. To investigate this effect, we have done the same simulation in a domain twice as wide ($W = 16$). The results are very much the same except for the phase lag along x. In the narrow domain ($W = 8$), patterns propagate from the sides toward the centre. In the wide domain, they appear to propagate from left to right. Therefore, the phase difference is indeed dependent on the sidewalls. The variation along x is milder for the wider channel, suggesting that the phase lag may disappear for very large W.

3.4. *Irregular patterns with disclinations ($Er > 145$)*

Figure 9 shows the histories of the velocity and director components at $Er = 200$. The initial stage of the birth and growth of the rolls is again similar to that in figure 3,
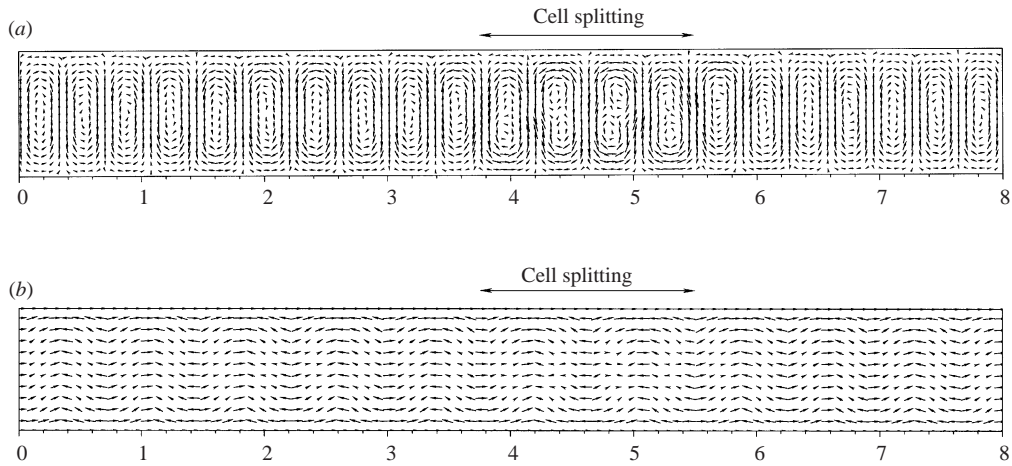
(*a*)

(*b*)

FIGURE 10. Cell splitting starts at $t = 40$ for $Er = 200$. (*a*) The flow field; (*b*) the director field.
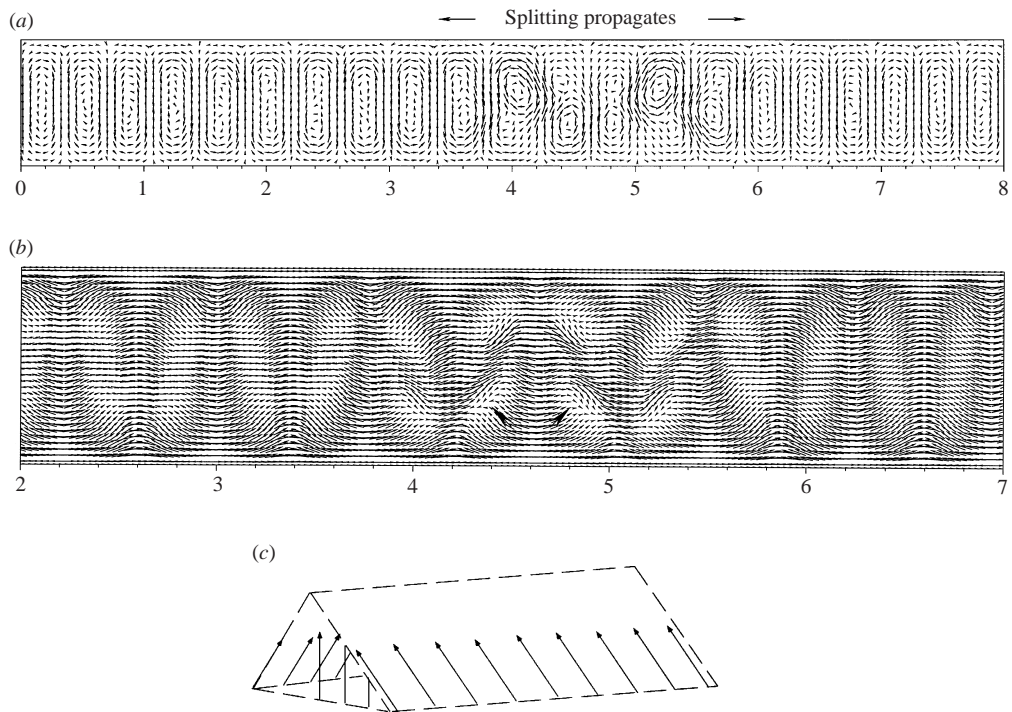
(*a*)

(*b*)

(*c*)

FIGURE 11. Cell splitting propagates to neighbouring cells at $t = 50$. (*a*) The flow field; (*b*) the director field. Note the butterfly pattern in the director field, and the appearance of ridges in the centre of the daughter cells (marked by large arrows). The ridge is sketched in three dimensions in (*c*).

though the process is more rapid. The cells are fully grown at $t \approx 30$ and have a wavenumber $q_x = 1.31$. Afterwards, the temporal variations become irregular. The spatial patterns at different times will be analysed in the following.

At $t = 40$ (figure 10), several rolls in the middle of the domain (roughly $3.7 < x <$ 5.5) start to split. The process is reminiscent of the splitting of oscillating rolls into
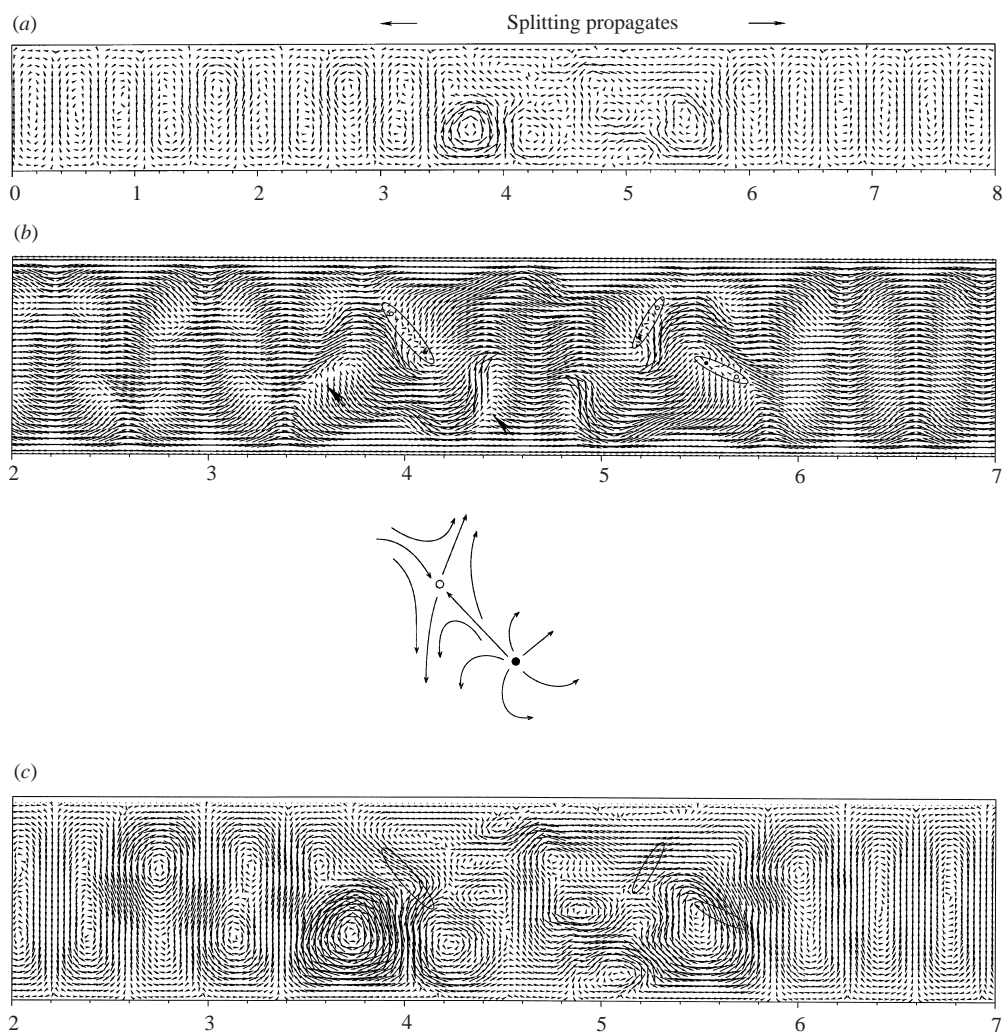
(*a*)

←— Splitting propagates —→

0   1   2   3   4   5   6   7   8

(*b*)

2   3   4   5   6   7

(*c*)

2   3   4   5   6   7

FIGURE 12. Cell splitting and secondary breakup lead to irregular patterns and three pairs of ± 1 disclinations at $t = 60$. (*a*) The whole flow field; (*b*) the director field. The large arrows point to two ridges, and the ellipses enclose pairs of defects, with open circles indicating -1 defect cores and filled circles $+1$ ones. At defect cores and the top of the ridges, $\boldsymbol{n}$ is in the flow direction, perpendicular to the page. The $\boldsymbol{n}$-field in the neighbourhood of one pair of defects is sketched. (*c*) Details of the flow field near the defects showing fast jet-like flows toward the $+1$ core.

dumbbells. But here the director and flow fields are synchronized, showing the same split pattern. The greatest tipping of $\boldsymbol{n}$ occurs at the core of the two 'daughter cells'. At $t = 50$ (figure 11), the splitting extends to the neighbouring cells, and the director field exhibits a characteristic butterfly pattern for the split cells. Particularly notable is the appearance of *ridges* at the centre of the split cells, indicated by the big arrows in figure 11(*b*), where the director orientation varies sharply. At the top of the ridges, the director is mostly aligned with the flow, perpendicular to the page. This is not apparent in the plot since the arrowheads representing $\boldsymbol{n}$ cannot be shrunk into a point. The ridges play an essential role in the formation of disclinations as discussed below.
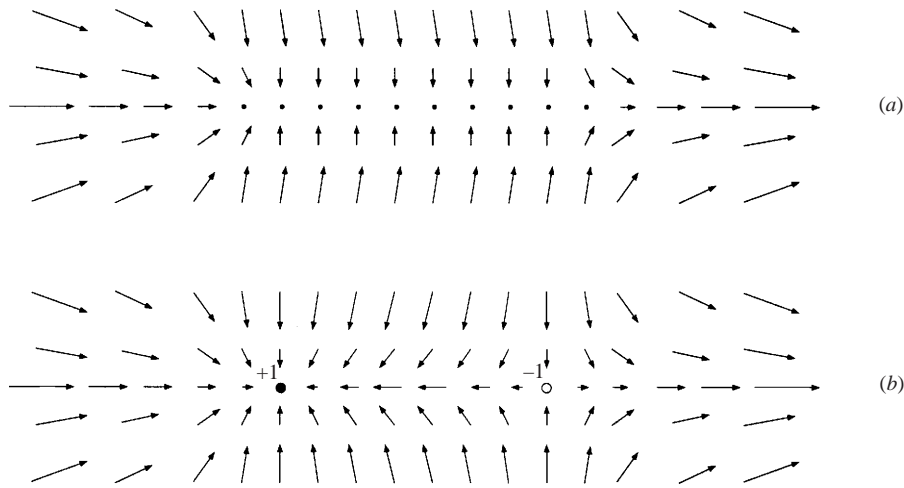
FIGURE 13. Cartoons showing the nucleation of a pair of disclinations from a ridge. (*a*) Top view of the ridge before splitting; (*b*) the ridge splits to create a pair of ± 1 defects in the escaped configuration.

At $t = 60$ (figure 12), the flow field exhibits a continuation of cell splitting towards the left and right, and the first sign of irregularity among the split cells. Some of the daughter cells have undergone secondary breakup, forming swirls of various sizes and strengths. The director field also becomes irregular, and the first disclinations have nucleated from the ridges. This process is illustrated by the cartoons in figure 13. During cell splitting and secondary breakup, some ridges are heightened, at the top of which the director essentially points in the flow direction (figure 13*a*). At its base, the ridge merges smoothly into the background *n*-field, which points to the right in this illustration. If the local flow is such as to sway *n* on the ridge to the right, the ridge will lower and smooth out. On the other hand, if the flow turns *n* to the left, the ridge splits to form a pair of ± 1 disclinations in the *escaped configuration* (figure 13*b*). To characterize the flow conditions conducive to ridge splitting, we compare the flow and orientation fields at the ridges in figures 12(*b*) and 12(*c*). After spatial irregularity sets in, the ridges are no longer located at the core of the eddies, as is the case for newly split cells. Instead, they almost always coincide with the faster and near-parallel flows between the eddies. In particular, ridge splitting is accompanied by a *jet-like flow*, with a strong stream, running roughly toward the $+1$ defect core, flanked by weaker flows (figure 12*c*). Conceivably, the shear in the jet turns *n* toward the $+1$ defect as sketched in figure 13(*b*). This scenario is prevalent in the simulations but not universal; sometimes a ridge splits where the flow crosses the line linking the two defect cores.

After formation, the defects are convected by the swirling flow, interacting with one another through distortional elasticity as well as hydrodynamically through modifying the flow field. Eventually, a defect will be attracted to another of the opposite strength, and the two will annihilate. The lifespan of a disclination is typically around 10 strain units, but can be as long as 30.

At $t = 100$ (figure 14), the last cells are being split next to the sidewalls, and the director field exhibits one pair of disclinations and several ridges. From this point onward, the flow and orientation states become quasi-stationary in the sense that the qualitative features remain unchanged despite constant temporal and spatial
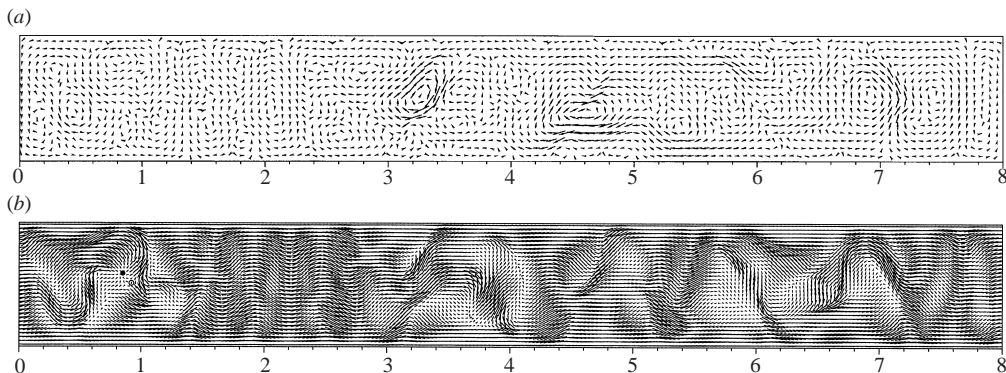
(a)

(b)

FIGURE 14. All cells are broken up by $t = 100$. (a) The flow field; (b) the director field.
There are numerous ridges and one pair of defects near $x = 0.9$.
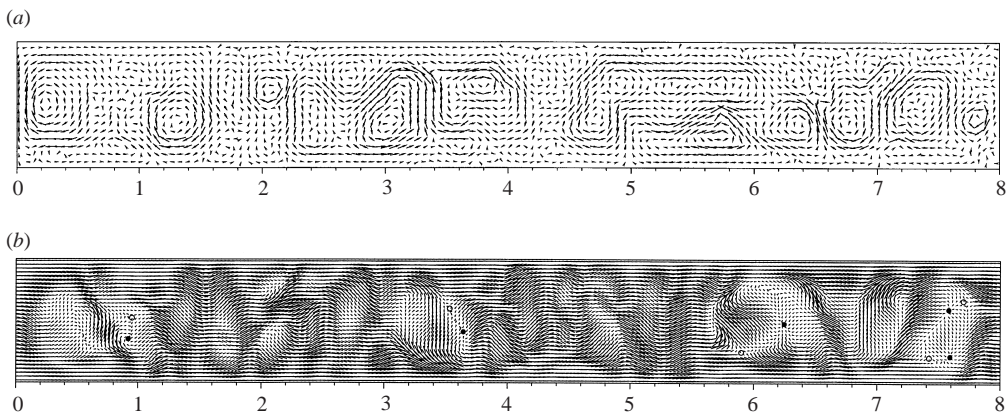
(a)

(b)

FIGURE 15. The quasi-stationary state at $t = 160$. (a) The flow field; (b) the director field
containing five pairs of defects and numerous ridges.

fluctuations. New ridges are raised and lowered, pairs of disclinations nucleating
and annihilating; eddies of various sizes form, break up and coalesce. Figure 15,
for $t = 160$, depicts such a quasi-stationary state. The flow field comprises eddies of
different sizes. The dominant feature is the large eddies with a diameter of roughly
$H/2$; the rest of the field consists of smaller eddies of half that size. The large
eddies have a more or less regular spacing of H, and the smaller ones are typically
$H/2$ apart. Thus, the flow and orientation fields are structured despite the apparent
randomness. This point will become clearer in § 4 when we compare the birefringent
pattern calculated from the director field in figure 15(b) with experiments.

The curious fact that cell breakup starts at an asymmetric position (figure 10)
suggests that the sidewalls may have introduced extraneous effects into the above
scenario. To investigate this effect, we have performed the same simulation in a wider
domain with $W = 16$. Regular roll cells first emerge with a wavenumber $q_x = 1.34$,
slightly larger than in figure 10. At $t = 40$, cell splitting begins at $x \approx 5$ and $x \approx 11$,
and propagates to neighbouring cells. Later development closely resemble that in the
narrower domain, although the right half lags the left half somewhat. These results
do not suggest a strong role for the sidewalls. First, the scenario of cell breakup, ridge
formation and defect nucleation does not depend on the sidewalls, and probably

reflects the true physics. Second, the location of initial roll splitting appears to have an intrinsic wavelength of $x \approx 5$, independent of the domain width. Third, the left–right asymmetry in the domain seems also to be an intrinsic property of the flow. This may have been caused by a symmetry-breaking instability, triggered, say, by numerical errors that are not perfectly symmetric.

To confirm the accuracy of the results in figures 10–15, especially the mechanism for defect nucleation, we have done the same simulation on a finer grid with half the mesh size. The result is qualitatively the same, but the evolution takes much longer. For instance, the first pair of defects nucleate at $t = 240$ compared with $t = 60$ in figure 12. This has to do with the fact that the finer mesh supplies smaller truncation errors that feed the growing instability. Similar trends have been observed in the other regimes of instability.

4. Comparison with experiments

The experimental work most relevant to our simulations is due to Larson & Mead (1993), who sheared nematic polybenzylglutamate (PBG) solutions at finely controlled speeds in a high-precision translational shear cell. Three differences exist between the conditions in the experiment and those in the simulations. First, the material constants of the PBG solutions are not known. In the simulations, we have adopted the viscosities that Larson (1993) suggested for the 'typical nematic polymer', which are estimations based on the Doi theory. For the PBG solutions, the elastic constant K_2, for twist, is believed to be much smaller than the other two constants. In our calculations, all three are assumed equal. Second, the simulations assume uniformity along the flow direction while the observations indicate that this is not always true (see below). Finally, wall anchoring is along the vorticity direction in the simulations. Larson & Mead (1993) used homeotropic anchoring and subjected the material to preshearing. This effectively aligns the director with the vorticity, presumably through the twist instability of Zuniga & Leslie (1989*a*), except for a boundary layer near the walls.

Despite these differences, the four regimes discovered in simulations seem to be consistent with observations. First, no roll cells appear in the experiment for sufficiently low shear rates; the simple shear flow is stable. This corresponds to our first regime. The critical Er^c for the onset of roll-cell instability is 55 in the simulations, almost exactly the value predicted by Larson's (1993) linear instability analysis. Since Larson (1993) used $K_1 = K_3 = 10K_2$, the agreement of Er^c indicates that the onset of roll cells is insensitive to a weaker twist constant, at least within the Leslie–Ericksen theory. This confirms a similar observation by Larson (1993) who varied K_3/K_2 between 2 and 10. Comparison with the experimental Er^c is made difficult by uncertainties in the value of the material constants for the PBG solutions (see p. 164 of Larson & Mead 1993 and the Corrigendum to that paper). Inferring a value of γ_1/K_1 from a similar solution, Larson & Mead defined an Ericksen number based on γ_1: $E_\gamma = \gamma_1 V H / K_1$. They estimated an experimental critical value $E_\gamma^c \approx 400$. If Er^c from Larson's (1993) linear theory (and our simulations) is converted using viscosities of the 'typical nematic polymer', one obtains $E_\gamma^c = 2368$, much higher than the experimental value. Larson & Mead (1993) attributed the discrepancy to differences in the viscosity ratios. In the following, we only make comparisons in terms of the Ericksen number ratio Er/Er^c.

In our second regime, roll cells appear and then grow monotonically to a steady
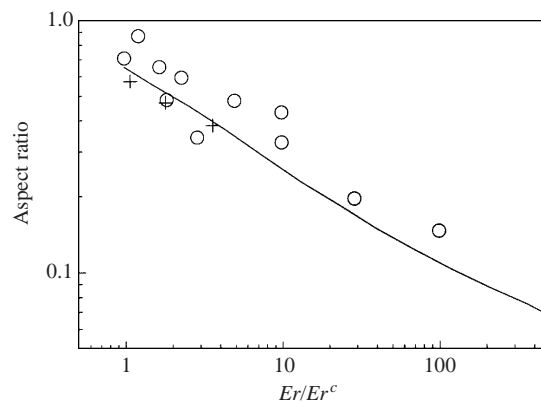
FIGURE 16. Comparison of the aspect ratio of the roll cells among three studies. The solid line represents the linear instability theory of Larson (1993), the circles are experimental measurements by Larson & Mead (1993), and the crosses are from our simulations.

state, maintaining the same wavenumber. Larson & Mead (1993) observed a similar regime of 'steady-state birefringence and phase grating':

> Thus the bifurcation to roll cells appears to be a supercritical one, and arbitrarily weak roll cells can be stabilized at values (of E_γ) only slightly above critical. Observation of the birefringence patterns in these weak roll cells... shows that the departure of the director from orientation in the vorticity direction toward the flow direction is small when the roll cells first appear, but increases continuously as (E_γ) is increased.

These observations apply equally well to our simulated roll cells.

Our third regime of oscillating roll cells has no apparent counterpart in the observations. This may be due to the fact that the oscillation between dumbbells and wrist-watches does not change the spatial periodicity along x, and hence should not affect the spacing between birefringent stripes. The temporal variations in light intensity may not be noticeable from visual observations and photographs of the stripes. To test this idea, we calculated the birefringence for the three times depicted in figure 6 (details of such calculations are given by Han & Rey 1995). Indeed, the position of the stripes does not change and the variation in light intensity is at most 15% during the oscillation. Based on this argument, we may consider the steady regime of Larson & Mead (1993) as consisting of our steady and oscillating regimes. Experimentally, this regime covers $1 < Er/Er^c < 3.5$. Numerically, the two regimes cover the range of $1 < Er/Er^c < 2.64$.

Figure 16 compares the aspect ratio of the rolls at various Ericksen number ratios from three separate studies: Larson's (1993) linear instability analysis, Larson & Mead's (1993) experimental measurements and our simulations. For higher Er, the rolls eventually become irregular in both the simulations and experiments (see discussion below). The high-Er data points, therefore, are taken from clearly defined roll cells at smaller strains. In all three studies, the rolls become narrower with increasing shear rates. The close agreement between the linear theory and our numerical data is expected since the wavenumber does not change during the nonlinear growth of the cells. The small discrepancy is probably attributable to the smaller K_2 used by Larson (1993), and to the limitation of a discrete number of cells in our computational domain. The agreement with experimental data, though tempered by the uncertainty in Er^c, is reasonably good.
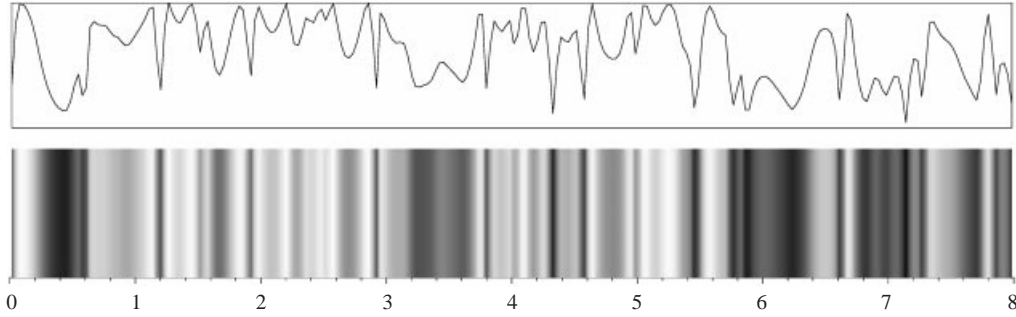
FIGURE 17. The birefringence pattern computed from the director field in figure 15(*b*). The top diagram shows the intensity of transmitted light, and the bottom represents that intensity by grey-scales. The polarizer is along the flow direction and the analyser along the vorticity. We assume a sample thickness of $100\,\mu$m and a wavelength of $630\,$nm and use the refractive indices of PBG given by Dupré (1982).

Finally, in our fourth regime, simulations at $Er = 200$ ($Er/Er^c = 3.64$) show that roll cells form and grow monotonically until about 40 strain units. At $t \approx 60$, thick disclinations nucleate out of rolls that have broken up; they persist for some 10 strain units before cancelling out. Eventually, the entire domain is filled with an irregular pattern consisting of swirls of various sizes. Experimentally, Larson & Mead (1993) recorded the evolution of birefringence patterns for $Er/Er^c = 5.25$. Stripes first appear at 8 strain units, and become 'sharply defined' at 18 strain units. Around this time, thick disclinations are first observed, and they seem to reside between the roll cells. 'The lines are of finite length, fading in intensity and disappearing as one follows them in space'. Thereafter, 'if shearing is prolonged for 50 or more strain units, a weaker fine structure appears, which disrupts somewhat the regularity of the striped pattern. As V increases, the fine structure becomes even more intense, and the pattern becomes less and less coherent'.

All the major events observed experimentally also appear to occur in the simulations, and in the correct order. In particular, the 'weaker fine structure' that develops after prolonged shearing can be identified with the small swirls that form after cell splitting and secondary breakup. To illustrate this, we have calculated the birefringence pattern that would be produced by the director field of figure 15(*b*). One may identify the 'primary stripes' as between sharply defined dark lines in figure 17. With a width typically between $0.7H$ and H, these stripes correspond to the large eddies in figure 15(*a*). Within the primary stripes there are short-wave fluctuations, creating irregular 'secondary stripes' which are finer and fainter. These can be attributed to the small eddies. Note that disclinations impart streamwise orientation to their surrounding areas, and hence tend to cause extinction of transmitted light. However, this is only a mild effect in figure 17 because the defect cores are small compared with the thickness of the sample. In particular, individual defect cores cannot be discerned from the calculated birefringence pattern. A global measure of the director orientation is $v = \langle n_z^2 \rangle - \langle n_x^2 \rangle$, where the bracket represents averaging over the entire domain. For the quasi-stationary state in figure 15, v fluctuates around -0.05. Therefore, the director field is still largely under the influence of the anchoring condition ($n_x = 1$) despite the streamwise alignment near defects and ridges. The latter effect is expected to intensify with increasing Er, eventually leading to a positive v. Indeed, Hongladarom *et al.*'s (1993) birefringence measurements indicate $v = 0.53$ for PBG solutions in the regime of director turbulence.

Unfortunately, the ridge-splitting mechanism for generating defects cannot be directly verified for lack of detailed observations at small length scales. In fact, mapping the fluctuating and non-uniform director field would present a great experimental difficulty. On a coarser level, we note a discrepancy in the location of disclinations. Larson & Mead (1993) determined that the defect lines are between roll cells, with a spacing roughly equal to the roll size. Mather *et al.* (1996*b*) recorded the nucleation of thick disclinations from roll cells for the small-molecule nematic 8CB in a torsional shear cell. The spacing between disclinations appears rather random. Some disclinations fall on cell boundaries and others are not parallel to the flow direction, traversing one or two cell widths within the length viewed. In our simulations, pairs of defects nucleate from ridges which have formed in the core of broken cells, and their spacing is irregular.

It is not clear how the two sets of experimental results can be reconciled, and whether the occurrence of defects away from the cell boundaries in Mather *et al.* (1996*b*) is related to our ridge-splitting mechanism. In this connection, we remind the reader of the different conditions in the experiments and the computations. The simulations assume no variations along the flow direction. Experimentally, the defect lines have a finite length. They are wavy in Larson & Mead (1993). Though apparently straight in Mather *et al.* (1996*b*), they sometimes cross the rolls at an angle. In either case, streamwise variations clearly exist. In addition, the simulations use wall anchoring in the vorticity direction, while both experiments had homeotropic anchoring. Larson & Mead (1993) noted that at the beginning of flow, 'the orientation is not completely uniform, and at the glass surfaces the director prefers a homeotropic orientation, with an unknown anchoring strength'. The distortion in the boundary layer near the wall may have played a role in the nucleation of defects in the experimental studies. Finally, the viscosities and elastic constants clearly differ between the PBG in Larson & Mead (1993) and the 8CB in Mather *et al.* (1996*b*); both are probably different from the values we have used here.

Note also that events occur at a more rapid pace in experiments than in simulations. This is probably due to the same reasons for the lower Er^c in experiments, which may include differing viscosity ratios and the spatial non-uniformities noted in the last paragraph. Another relevant fact is that the evolution of instabilities depends greatly on the nature and magnitude of the disturbances supplied to the system. For example, numerical experiments show that a faster and shorter evolution can be achieved by using larger disturbances. On the other hand, the onset, growth and eventual breakup of roll cells all take longer if the mesh is refined.

At still higher shear rates ($E_\gamma \sim 10^5$), Larson & Mead (1993) observed that the striped pattern is all but obscured by temporal fluctuations and spatial irregularities. This is termed 'director turbulence', whose similarities and contrast to inertial turbulence have long been a topic of interest (e.g. Gähwiller 1972; Manneville 1981; Larson 1993). Our simulations assume no variation along the flow direction, and thus cannot represent truly three-dimensional structures in director turbulence.

5. Concluding remarks

Within the parameter ranges covered, numerical simulations based on the Leslie–Ericksen theory have revealed a series of instabilities in sheared nematics leading to irregular orientational patterns with defects. Four flow regimes can be demarcated:
A. Stable simple shear ($Er < 55$).
B. Steady roll cells ($55 < Er < 85$). As expected, the onset of roll cells is very much

like the predictions of Larson's (1993) linear theory. The nonlinear growth of rolls, however, is remarkably uneventful.

C. Oscillating roll cells ($85 < Er < 145$). At least two neighbouring modes may be amplified, resulting in non-unique solutions in this regime.

D. Irregular patterns with disclinations ($Er > 145$). Through cell splitting and breakup, ridges form where the director is swept into the flow direction. Favourable local flow conditions then split the ridge to create a pair of ± 1 disclinations.

Comparison with experiments is limited to the gross features amenable to visual observations. The four regimes are generally consistent with experimental observations. However, the location of disclinations differs between experiments and simulations. In addition, the mechanism for nucleating disclinations cannot be directly checked by observations at the present level of resolution.

Perhaps the most important result of this paper is the discovery of a mechanism for generating disclinations in shear flows. This may not be the only scenario leading to shear-induced defects. We have only considered defects generated in the flowing bulk. Yan *et al.* (1994) and Mather *et al.* (1996*a*) have observed disclinations nucleating near walls with homeotropic anchoring. The physical mechanism for this is unknown. Besides, Mather *et al.* (1996*b*) documented bulk nucleation of disclinations in a narrow Er range prior to the formation of roll cells. This is perhaps related to their torsional flow geometry since a similar phenomenon was not seen in the planar shear of Larson & Mead (1993).

The numerical work reported here is limited by the Leslie–Ericksen theory to slow flows and mild distortions. Hence, the defects produced are all of the escaped type with relatively smooth cores. Fortunately, experiments indicate that only thick lines nucleate from roll cells in shearing flows (Larson & Mead 1993; Mather *et al.* 1996*b*). In more complex flow geometries, however, $\pm 1/2$ defects have been experimentally observed (e.g. Wood & Thomas 1986). Such 'thin' disclinations cannot escape into the third dimension and the core cannot be represented by the Leslie–Ericksen theory. Evidently, a 'molecular theory' is needed which accounts not only for the rotation of the director $\boldsymbol{n}$, but also for the changes in the orientation distribution function and the concomitant viscoelasticity. Using the Doi theory, Feng & Leal (1997) showed that $\pm 1/2$ defects with smooth cores occur in inhomogeneous flows. The Doi theory is deficient in that it neglects distortional elasticity. This has been remedied by Feng *et al.* (2000) in a more general molecular theory, which is being used in shear and complex flow simulations (cf. Sgalari *et al.* 2000).

REFERENCES

ALDERMAN, N. J. & MACKLEY, M. R. 1985 Optical textures observed during the shearing of thermotropic liquid-crystal polymers. *Faraday Discuss. Chem. Soc.* **79**, 149–160.

BURGHARDT, W. R. & FULLER, G. G. 1990 Transient shear flow of nematic liquid crystals: manifestations of director tumbling. *J. Rheol.* **34**, 959–992.

CARLSSON, T. 1984 Theoretical investigation of the shear flow of nematic liquid crystals with the Leslie viscosity $\alpha_3 > 0$: hydrodynamic analogue of first order phase transitions. *Mol. Cryst. Liq. Cryst.* **104**, 307–334.

Donald, A. M. & Windle, A. H. 1992 *Liquid Crystalline Polymers*. Cambridge University Press.

Dupré, D. B. 1982 Techniques for the evaluation of material constants in lyotropic systems and the study of pretransitional phenomena in polymer liquid crystals. In *Polymer Liquid Crystals* (ed. A. Ciferri, W. R. Krigbaum & R. B. Meyer), chap. 7. Academic.

Feng, J. & Leal, L. G. 1997 Numerical simulations of the flow of dilute polymer solutions in a four-roll mill, *J. Non-Newtonian Fluid Mech.* **72**, 187–218.

Feng, J. J., Sgalari, G. & Leal, L. G. 2000 A theory for flowing nematic polymer with orientational distortion. *J. Rheol.* **44**, 1085–1101.

Gähwiller, C. 1972 Temperature dependence of flow alignment in nematic liquid crystals. *Phys. Rev. Lett.* **28**, 1554–1556.

de Gennes, P. G. & Prost, J. 1993 *The Physics of Liquid Crystals* 2nd Edn. Oxford University Press.

Hackbusch, W. & Trottenberg, U. 1982 *Multigrid Methods*. Springer.

Han, W. H. & Rey, A. D. 1994a Dynamic simulations of shear-flow-induced chirality and twisted-texture transitions of a liquid-crystalline polymer. *Phys. Rev. E* **49**, 597–613.

Han, W. H. & Rey, A. D. 1994b Orientation symmetry breakings in shearing liquid crystals. *Phys. Rev. E* **50**, 1688–1691.

Han, W. H. & Rey, A. D. 1994c Simulation and validation of nonplanar nematorheology. *J. Rheol.* **38**, 1317–1334.

Han, W. H. & Rey, A. D. 1995 Theory and simulation of optical banded textures of nematic polymers during shear flow. *Macromolecules* **28**, 8401–8405.

Hongladarom, K., Burghardt, W. R., Baek, S. G., Cementwala, S. & Magda, J. J. 1993 Molecular alignment of polymer liquid crystals in shear flows. 1. Spectrographic birefringence technique, steady-state orientation, and normal stress behavior in poly(benzyl glutamate) solutions. *Macromolecules* **26**, 772–784.

Kupferman, R., Kawaguchi, M. N. & Denn, M. M. 2000 Emergence of structure in a model of liquid crystalline polymers with elastic coupling. *J. Non-Newtonian Fluid Mech.* **91**, 255–271.

Larson, R. G. 1993 Roll-cell instabilities in shearing flows of nematic polymers. *J. Rheol.* **37**, 175–197.

Larson, R. G. & Mead, D. W. 1992 Development of orientation and texture during shearing of liquid-crystalline polymers. *Liq. Cryst.* **12**, 751–768.

Larson, R. G. & Mead, D. W. 1993 The Ericksen number and Deborah number cascades in sheared polymeric nematics. *Liq. Cryst.* **15**, 151–169; and Corrigendum **20**, 265 (1996).

Manneville, P. 1981 The transition to turbulence in nematic liquid crystals. *Mol. Cryst. Liq. Cryst.* **70**, 223–250.

Manneville, P. & Dubois-Violette, E. 1976 Shear flow instability in sheared nematic liquids: theory steady simple shear flows. *J. Phys. Paris* **37**, 285–296.

Mather, P. T., Pearson, D. S. & Larson, R. G. 1996a Flow patterns and disclination-density measurements in sheared nematic liquid crystals. I. Flow-aligning 5CB. *Liq. Cryst.* **20**, 527–538.

Mather, P. T., Pearson, D. S. & Larson, R. G. 1996b Flow patterns and disclination-density measurements in sheared nematic liquid crystals. II. Tumbling 8CB. *Liq. Cryst.* **20**, 527–538.

Müller, J. A., Stein, R. S. & Winter, H. H. 1996 Rotation of liquid crystalline macromolecules in shear flow and shear-induced periodic orientation patterns. *Rheol. Acta* **35**, 160–167.

Patankar, S. V. 1980 *Numerical Heat Transfer and Fluid Flow*. Hemisphere.

Pieranski, P. & Guyon, E. 1976 Shear flow instabilities in nematic CBOOA. *Commun. Phys.* **1**, 45–49.

Sgalari, G., Leal, L. G. & Feng, J. J. 2000 The flow behavior of LCPs based on a generalized Doi model with distortional elasticity. *Proc. XIIIth Intl Congr. Rheol., Cambridge, UK* (ed. D. M. Binding, N. E. Hudson, J. Mewis, J.-M. Piau, C. J. S. Petrie, P. Townsend, M. H. Wagner & K. Walters), Vol. 3, pp. 239–241. British Society of Rheology, Glasgow.

Srinivasarao, M. & Berry, G. C. 1991 Rheo-optical studies on aligned nematic solutions of a rodlike polymer. *J. Rheol.* **35**, 379–397.

Vanka, S. P. 1986 Block-implicit multigrid solution of Navier-Stokes equations in primitive variables. *J. Comput. Phys.* **65**, 138–158.

Wood, B. A. & Thomas, E. L. 1986 Are domains in liquid crystalline polymers arrays of disclinations? *Nature* **324**, 655–657.

YAN, N. X., LABES, M. M., BAEK, S. G. & MAGDA, J. J. 1994 Shear-induced textures in the lyotropic liquid crystal poly(γ-benzyl L-glutamate) (PBLG). *Macromolecules* **27**, 2784–2788.

ZUNIGA, I. & LESLIE, F. M. 1989*a* Shear flow instabilities in nonaligning nematic liquid crystals. *Europhys. Lett.* **9**, 689–693.

ZUNIGA, I. & LESLIE, F. M. 1989*b* Shear-flow instabilities in non-flow-aligning nematic liquid crystals. *Liq. Cryst.* **5**, 725–734.